Geophysical Research Letters

RESEARCH LETTER
10.1029/2020GL086970

Contrasting Scale Dependence of Entrainment-Mixing Mechanisms in Stratocumulus Clouds

Sinan Gao[1], Chunsong Lu[1], Yangang Liu[2], Fan Mei[3], Jian Wang[2,4], Lei Zhu[1], and Shuqi Yan[1]

[1]Collaborative Innovation Center on Forecast and Evaluation of Meteorological Disasters, Key Laboratory for Aerosol-Cloud-Precipitation of China Meteorological Administration, Nanjing University of Information Science and Technology, Nanjing, China, [2]Environmental and Climate Sciences Department, Brookhaven National Laboratory, Upton, NY, USA, [3]Pacific Northwest National Laboratory, Richland, WA, USA, [4]Center for Aerosol Science and Engineering, Department of Energy, Environmental and Chemical Engineering, University of Washington, St. Louis, WA, USA

Key Points:
- Entrainment-mixing mechanisms can become more homogeneous or inhomogeneous with increasing averaging scales
- Scale dependence sign and strength are related to microphysical properties, entrained air relative humidity, and droplet-free air fraction
- A new heuristic model and two new dimensionless parameters are introduced to quantify the scale dependence

Supporting Information:
- Supporting Information S1

Correspondence to:
C. Lu and Y. Liu,
luchunsong110@gmail.com;
lyg@bnl.gov

Citation:
Gao, S., Lu, C., Liu, Y., Mei, F., Wang, J., Zhu, L., & Yan, S. (2020). Contrasting scale dependence of entrainment-mixing mechanisms in stratocumulus clouds. *Geophysical Research Letters*, *47*, e2020GL086970. https://doi.org/10.1029/2020GL086970

Received 8 JAN 2020
Accepted 14 APR 2020
Accepted article online 17 APR 2020

Abstract The apparent turbulent entrainment-mixing mechanism between clouds and surrounding air is scale dependent; however, such scale dependence has been rarely studied, hindering development of scale-aware entrainment-mixing parameterizations. Here we extend our previous study on cumulus clouds to investigate scale dependence of entrainment-mixing processes in stratocumulus clouds during Aerosol and Cloud Experiments in Eastern North Atlantic and Routine AAF (Atmospheric Radiation Measurement (ARM) Aerial Facility) Clouds with Low Optical Water Depths (CLOWD) Optical Radiative Observations (RACORO). In contrast to previous studies, two opposite scale dependencies are found: Entrainment mixing can become more homogeneous or more inhomogeneous with increasing averaging scales, which is quantified by the difference between homogeneous mixing degree at the 100 and 10 m resolutions. A new heuristic model and two new quantities are introduced. The observations and model show that microphysical properties near and far away from droplet-free air and relative humidity of entrained air determine both the sign and strength of scale dependence, while droplet-free air fraction only affects the strength. The results shed new light on developing scale-aware parameterizations of entrainment-mixing mechanisms.

Plain Language Summary Turbulent entrainment mixing between clouds and surrounding air significantly affects cloud microphysical properties over a wide range of scales, indicating that the apparent entrainment-mixing mechanism is scale dependent. Previous studies have shown that entrainment-mixing mechanisms tend to be more inhomogeneous when the sampling rate is lower. Surprisingly, the present study shows two opposite behaviors of scale dependence: The mechanisms can become more homogeneous or more inhomogeneous. To understand the physical mechanisms responsible for the scale dependence, a new heuristic model is established. Cloud microphysics and relative humidity of the entrained air determine both the sign and strength of scale dependence, while droplet-free air fraction only determines the strength. Two new quantities combining all the factors are defined, and they can better quantify the effects of the factors on scale dependence than each individual factor. This study finds a new phenomenon of scale dependence and improves our physical understanding of entrainment mixing.

1. Introduction

About two thirds of the Earth's surface is covered by clouds which have been considered as a major source of uncertainty in climate research (Bony & Dufresne, 2005; Cess et al., 1989; Stephens, 2005; Wang, 2015). The interactions between clouds and their environmental air through turbulent entrainment-mixing processes have been studied for several decades (Liu et al., 2002; Yum, 1998), because these processes have significant effects on cloud-climate feedbacks, aerosol indirect effect evaluation, and warm-rain initiation (Ackerman et al., 2004; Del Genio & Wu, 2010; Kim et al., 2008; Kumar et al., 2013; Liu et al., 2002; Stanfield et al., 2019; Xue & Feingold, 2006; Yang et al., 2019; Zheng et al., 2015).

Despite tremendous efforts in the past few decades, our understanding of turbulent entrainment-mixing mechanisms is still far from complete. Some observations suggested that the entrainment-mixing

processes were close to homogeneous (Burnet & Brenguier, 2007; Gerber et al., 2008; Jensen et al., 1985; Lu et al., 2013), whereas others pointed to the extreme inhomogeneous scenario (Burnet & Brenguier, 2007; Freud et al., 2008; Freud et al., 2011; Haman et al., 2007; Lu et al., 2011; Pawlowska et al., 2000) or a scenario between the two extremes (Lehmann et al., 2009; Lu et al., 2014). Some simulations (Chosson et al., 2007; Grabowski, 2006; Lasher-trapp et al., 2005; Yang et al., 2016) found that assuming different entrainment-mixing mechanisms led to significant difference in cloud albedo and/or large droplet formation; others (Hill et al., 2009; Morrison & Grabowski, 2008; Slawinska et al., 2012) found that the effects were weak. Recently, Hoffmann and Feingold (2019) developed an approach to simulate subgrid-scale turbulence fluctuation of supersaturation and claimed that cloud microphysics was more sensitive to entrainment-mixing mechanisms than in previous studies (e.g., Hill et al., 2009).

One of the major challenges behind the uncertainties of entrainment-mixing studies is that the related processes occur over a tremendous range of scales (Su et al., 1998), and the apparent entrainment-mixing mechanisms are scale dependent (Burnet & Brenguier, 2007; Kumar et al., 2018; Lu et al., 2014). Studying scale dependence of entrainment-mixing mechanisms is critical to developing scale-aware parameterizations, which is key to improve climate/weather models at different resolutions (Jeworrek et al., 2019; Xie & Zhang, 2015; Yun et al., 2017).

In Lu et al. (2014), we analyzed the cumulus data from the Routine AAF (Atmospheric Radiation Measurement (ARM) Aerial Facility) Clouds with Low Optical Water Depths (CLOWD) Optical Radiative Observations (RACORO) campaign and discussed the factors potentially affecting scale dependence strength without providing detailed physical explanations. Here we extend that work by examining the scale dependence in stratocumulus clouds, examining the controlling factors in detail, and improving physical understanding. The stratocumulus data collected during the Aerosol and Cloud Experiments in Eastern North Atlantic (ACE-ENA) and RACORO campaigns are analyzed. Different from Lu et al. (2014), two opposite scale dependence types are found: Entrainment-mixing mechanisms can become more homogeneous or more inhomogeneous, as averaging scales increase. A new heuristic model is established to explain the physical mechanisms responsible for the two opposite scale dependence types. Section 2 briefly describes the ACE-ENA and RACORO data set and definition of homogeneous mixing degree (ψ). Section 3 presents the scale dependence of ψ, and the heuristic model for analyzing the factors and mechanisms affecting the scale dependence. Section 4 presents concluding remarks.

2. Data Set and Methods

2.1. Data Set

During the ACE-ENA campaign, the Atmospheric Radiation Measurement Aerial Facility Gulfstream-1 aircraft was deployed during two intensive operational periods of early summer (June to July) of 2017 and winter (January to February) of 2018, respectively. Flights were carried out in the vicinity of an atmospheric observatory (i.e., ENA site) on Graciosa Island in the Azores, Portugal (39°5′30″N, 28°1′32″W, 30.48 m above mean sea level). The aircraft flew with a speed of 100 m s^{-1}. The cloud droplet size distributions (CDSDs) were measured by a Fast Cloud Droplet Probe at 10 Hz. The Fast Cloud Droplet Probe counts cloud droplets in 19 size bins, with bin centers ranging from 1.13 to 24 μm in radius. Humidity was measured with Open Path Tunable Diode Laser Hygrometer (Diskin et al., 2002) at 10 Hz. Air temperature, air pressure, and altitude were measured with the Aircraft Integrated Meteorological Measurement System at 20 Hz. Also analyzed are the stratocumulus data collected during the RACORO campaign at the Southern Great Plains site from January to June 2009 (Vogelmann et al., 2012; Yeom et al., 2017). The aircraft flew with a speed of 50 m s^{-1}. The CDSDs were measured by a Cloud and Aerosol Spectrometer with 10 Hz. The data with a bin-averaged radius larger than 1 μm are used. A Rosemount probe and the Tunable Diode Laser probe were used to measure temperature and water vapor at 10 Hz.

The key microphysical properties are calculated from CDSDs, including liquid water content (LWC_c), droplet number concentration (N_c), and mean volume radius (r_{vc}). A cloud record is defined with the criteria of $N_c > 10$ cm^{-3} and $LWC_c > 0.001$ g m^{-3}. This study only focuses on nondrizzling clouds with the criteria that the in-cloud drizzle water content of the Cloud Imaging Probe measurements (radius > 25 μm) averaged over the observation period is less than 0.005 g m^{-3}. In ACE-ENA, a total of 48 horizontal flight legs during

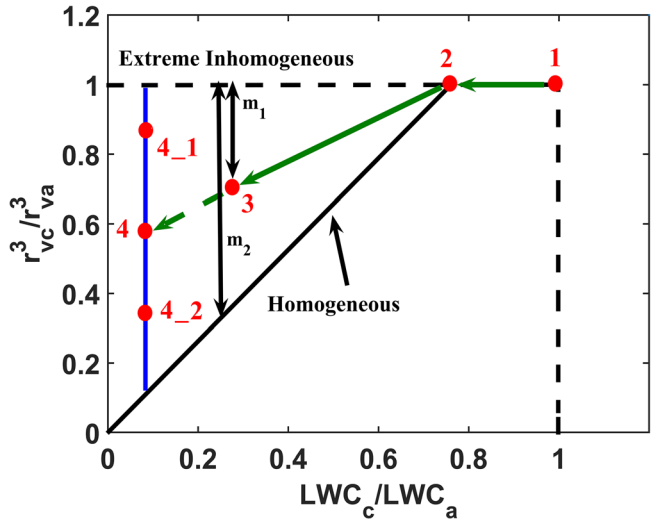

Figure 1. Diagram illustrating the definition of homogeneous mixing degree and scale dependence of homogeneous mixing degree. The horizontal dashed line represents extreme inhomogeneous mixing, and the solid line corresponds to homogeneous mixing. State 1 is an adiabatic state with mean volume radius of r_{va} and liquid water content of LWC_a. State 2 is just after entrainment but before mixing and evaporation, which has mean volume radius of r_{va} and liquid water content of $LWC_a \times \chi$, where χ is the mixing fraction of adiabatic cloud. State 3 is the state where new saturation is achieved after mixing and evaporation using the 100 m resolution data, with mean volume radius of r_{vc} and liquid water content of LWC_c. States 4, 4_1, and 4_2 are similar to State 3 but for the 10 m resolution. See text for the meanings of the other lines and symbols.

15 flights (21, 26, 28, and 30 June; 4, 6, 7, 8, and 13 July 2017; 26, 29, and 30 January; and 1, 7, and 10 February 2018) satisfies the above criteria. In RACORO, there are 21 qualified flight legs in seven flights (6, 8, 17, and 26 February; 20 March; 19 April; and 6 May 2009).

2.2. Methods

Entrainment-mixing mechanisms often fall between the homogeneous mixing and extreme inhomogeneous mixing. Lu et al. (2014) defined such a continuous measure that can encompass all types of mixing mechanisms based on the microphysical mixing diagram of r_{vc}^3/r_{va}^3 versus LWC_c/LWC_a,

$$\psi = \frac{m_1}{m_2} = \frac{1 - \frac{r_{vc}^3}{r_{va}^3}}{1 - \frac{1}{\chi}\frac{LWC_c}{LWC_a}}, \quad (1)$$

where m_1 and m_2 represent the lengths of two lines shown in Figure 1, respectively, r_{vc} and r_{va} are the mean volume radius and adiabatic mean volume radius, respectively, and LWC_c and LWC_a are the mean liquid water content and adiabatic liquid water content, respectively (Figure 1); χ is the mixing fraction of adiabatic cloud, which is calculated based on the conservation of total water and energy during the isobaric mixing at the aircraft observation level (Gerber et al., 2008; Lehmann et al., 2009; Lu et al., 2012). It is expected that ψ ranges from 0 to 1 and a larger value of ψ indicates a higher probability of homogeneous mixing.

3. Results

3.1. Scale Dependence of Homogeneous Mixing Degree

Cloud microphysical properties along 69 legs are used to calculate ψ. To study the dependence of ψ on the averaging scale, the averaging distance window (D) is set to be 10, 20, 30, 40, 50, 60, 70, 80, 90, 100, 200, 300, 400, 500, 600, 700, 800, 900, 1,000, 1,500, 2,000, 3,000, 4,000, 5,000, 6,000, 7,000, and 8,000 m; D is estimated with the aircraft flight speeds and averaging time (t) (Figure 2). The mean values of r_{vc} and LWC_c of each leg are used to calculate ψ. Two opposite behaviors of scale dependence exist. Figures 2a and 2c show the examples of ψ decreasing with the increasing D along one leg on 26 June 2017, during ACE-ENA, and on 6 February 2009, during RACORO, respectively. Scale dependence on D from several meters to several kilometers could be useful for developing parameterizations in models with different resolutions. A total of 51 horizontal legs has a similar behavior of ψ versus D. These results are consistent with previous studies (Lu et al., 2014), and this group is referred to as DECREASE legs. Figures 2b and 2d show the examples of opposite results whereby ψ increases with the increasing scale along one leg on 21 June 2017, during ACE-ENA, and on 20 March 2009, during RACORO, respectively. A total of 18 horizontal legs shares such a contrasting behavior, and this group is hereafter referred to as INCREASE legs. Figure S1 in the supporting information shows the variation ranges of ψ during the averaging processes. The range of ψ along the INCREASE legs is about one third of that along the DECREASE legs, not negligible, and one INCREASE leg still has the range larger than 0.1. Furthermore, understanding of the INCREASE legs could be even more important for other properties. For example, as shown in Figure S2, the INCREASE legs have much more significant scale dependence of r_{vc} than the DECREASE legs.

To further quantify the scale dependence, the relationship between ψ and D in Figure 2 is well fitted by the power law equation

$$\psi = a \times D^b + c, \quad (2)$$

where a, b, and c are three fitting parameters. The main difference is that a is positive for the INCREASE legs and negative for the DECREASE legs. The relationship between ψ and t in RACORO was fitted by the

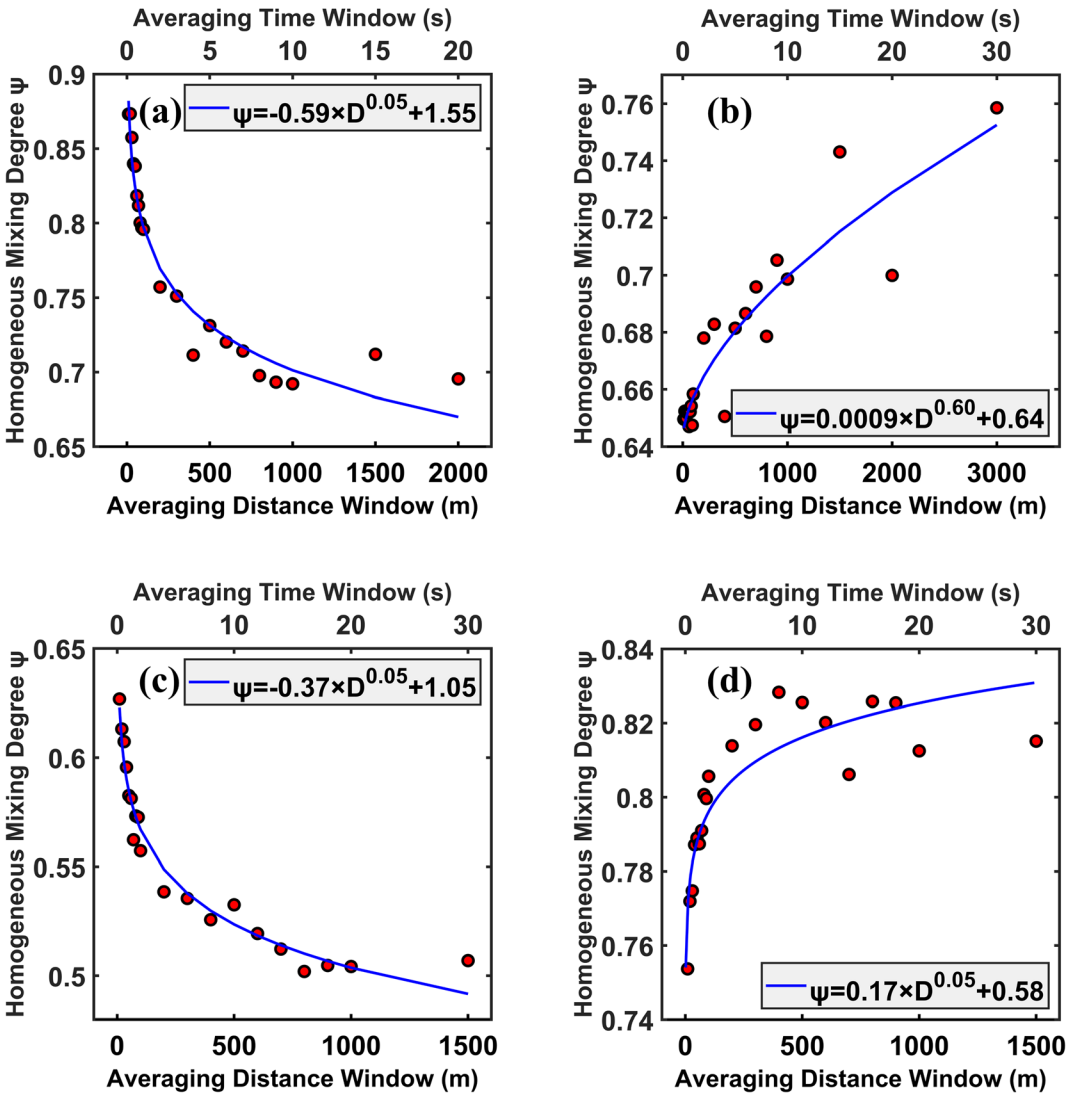

Figure 2. Examples of homogeneous mixing degree (ψ) as a function of averaging distance (D)/time (t) on (a) 26 June 2017, (b) 21 June 2017 during ACE-ENA, (c) 6 February 2009, and (d) 20 March 2009 during RACORO. The legends provide the fitting equations.

exponential function, $\psi = a+b \times c^t$, in Lu et al. (2014). The shapes of the two equations are similar, but the power law function would be more convenient to be used in the fractal analysis in future studies.

Two points are noteworthy. First, Lu et al. (2014) tested two methods to calculate mean ψ along each leg and the results were similar. Therefore, only one method is applied here: Mean r_{vc} and LWC_c are calculated first for different D and then ψ is calculated. Second, droplet-free air can be included in the calculations of r_{vc} and LWC_c with increasing D, where a droplet-free air blob refers to droplet-free air between two neighbor CDSDs. As D increases, less and less droplet-free air blobs remain. When D increases to a certain value (D_c), there would be no droplet-free air during averaging for $D > D_c$; it is expected that ψ does not vary with further increasing D. Therefore, ψ for $D > D_c$ is not calculated. The mean D_c by averaging all D_c of INCREASE and DECREASE legs is 1,010 m with its minimum and maximum values of 50 and 8,000 m, respectively.

3.2. Mechanisms Affecting Scale Dependence

Lu et al. (2014) gave the characteristics of negative scale dependence and the affecting factors but did not examine the mechanisms underlying the scale dependence. Figure 1 is plotted to dissect the mechanisms

responsible for the different behaviors of ψ when D increases. The difference between ψ at the resolutions of 100 m (ψ_{100m}) and 10 m (ψ_{10m}), $\psi_{100m} - \psi_{10m}$, is used to quantify the intensity of scale dependence. There are two reasons for using $\psi_{100m} - \psi_{10m}$. First, using this quantity is convenient to compare scale dependence strength along different legs. Second, 100 and 10 m are two commonly used sampling rates in aircraft campaigns for the aircraft speed of 100 m s^{-1}, and CDSDs averaged over 10 m (10 Hz) and 100 m (1 Hz) have more samples than for other averaging scales, for example, 1,000 m. Point 1 has adiabatic values, r_{va} and LWC_a. Point 2 has r_{va} and $LWC_a \times \chi$, which is a state just after entrainment but before evaporation. After mixing and evaporation, the cloud achieves new saturation, that is, Point 3. If Point 3 with the original 10 m resolution data moves to Point 4 with averaged 100 m resolution data along the dash arrow, it is easy to prove that ψ is constant with the theorem of similar triangles. If Point 3 moves to Point 4_1 after averaging, $\psi_{100m} - \psi_{10m} < 0$; if Point 3 moves to Point 4_2 after averaging, $\psi_{100m} - \psi_{10m} > 0$. Therefore, the slopes of the line linking Points 2 and 3 (k_{23}) and the line linking Points 2 and 4 (k_{24}) are critical to determining the sign and strength of scale dependence. The mean k_{24} (1.36) of the DECREASE legs is smaller than the mean k_{23} (1.44), and the mean k_{24} (0.64) of the INCREASE legs is larger than the mean k_{23} (0.62).

A new heuristic model is presented to understand the factors that affect these slopes. According to its definition, ψ is positively correlated with LWC_c and negatively correlated with r_{vc}^3, others being equal. Therefore, the scale dependence of ψ is related to LWC_c and r_{vc}^3 at the resolutions of 10 m (LWC_{c10m} and r_{vc10m}) and 100 m (LWC_{c100m} and r_{vc10m}). The microphysical properties far away from and near droplet-free air are expected to play different roles in the averaging processes. Therefore, it is essential to separate the microphysics into two groups. The microphysical properties with subscripts 1 and 2 indicate the properties far away from and near droplet-free air, respectively. According to the property on the y axes of Figure 1, $r_{vc100m}^3 - r_{vc10m}^3$ should be derived, but its form is complicated. Since $r_{vc100m}^3 - r_{vc10m}^3$ is proportional to $r_{vc100m} - r_{vc10m}$, here $r_{vc100m} - r_{vc10m}$ is derived to evaluate the variation trend of $r_{vc100m}^3 - r_{vc10m}^3$:

$$r_{vc100m} - r_{vc10m} = -x\,(r_{v1} - r_{v2}). \tag{3}$$

Similarly,

$$LWC_{c100m} - LWC_{c10m} = -x\ LWC_1 - y\ LWC_2, \tag{4}$$

where x and y are positive and increasing functions of droplet-free air blob size (S); see the supporting information for detailed derivation. Based on equations 3 and 4, $r_{vc100m} - r_{vc10m}$ can be positive or negative and $LWC_{c100m} - LWC_{c10m}$ must be negative (Figure S2). In Lu et al. (2014), we only examined the effects of cloud microphysical properties near droplet-free air (quantities with subscript 2). However, the cloud microphysical properties far away from droplet-free air also affect the scale dependence of ψ, as revealed by equations 3 and 4.

To confirm this analysis, Figures 3a–3c show the relationships of $\psi_{100m} - \psi_{10m}$ to $(r_{v1} - r_{v2})/r_{vc}$, LWC_1/LWC_c, and LWC_2/LWC_c, respectively. The CDSDs from the left side and the one from the right side adjacent to each droplet-free air blob are averaged to calculate r_{v2} and LWC_2. The remaining CDSDs far away from droplet-free air are used to calculate r_{v1} and LWC_1. Because different clouds have significantly different r_{vc} and LWC_c, the normalized parameters of $(r_{v1} - r_{v2})/r_{vc}$, LWC_1/LWC_c, and LWC_2/LWC_c are thought to be more reasonable to study microphysical effects on the scale dependence of ψ. Also shown are the relationships of $\psi_{100m} - \psi_{10m}$ to RH (Figure 3d) and droplet-free air fraction ($L_{fraction}$) defined as the fraction of droplet-free data points to the sum of droplet-free and cloud data points (Figure 3e). Note that droplet-free air (represented by $L_{fraction}$) is not equivalent to dry air entrained into cloud. For example, when a dry air blob is entrained into cloud, cloud droplets evaporate partially and saturate the dry air blob. Finally, the saturated "dry air" contains cloud droplets. In this case, $L_{fraction}$ is 0, not equivalent to the dry air blob size. Figure 3 well captures the contrasting correlation between $\psi_{100m} - \psi_{10m}$ and $L_{fraction}$: positive for INCREASE legs and negative for DECREASE legs, which is consistent with the heuristic model (Figure S3). The heuristic model also shows that the INCREASE and DECREASE legs have the same correlation signs between $\psi_{100m} - \psi_{10m}$ and $(r_{v1} - r_{v2})/r_{vc}$, LWC_1/LWC_c, LWC_2/LWC_c, and RH (Figure S3); the blue fitting lines in Figure 3 (a combination of the INCREASE and DECREASE legs) are consistent with the model. Considering the INCREASE and DECREASE legs separately, most of the correlation signs in

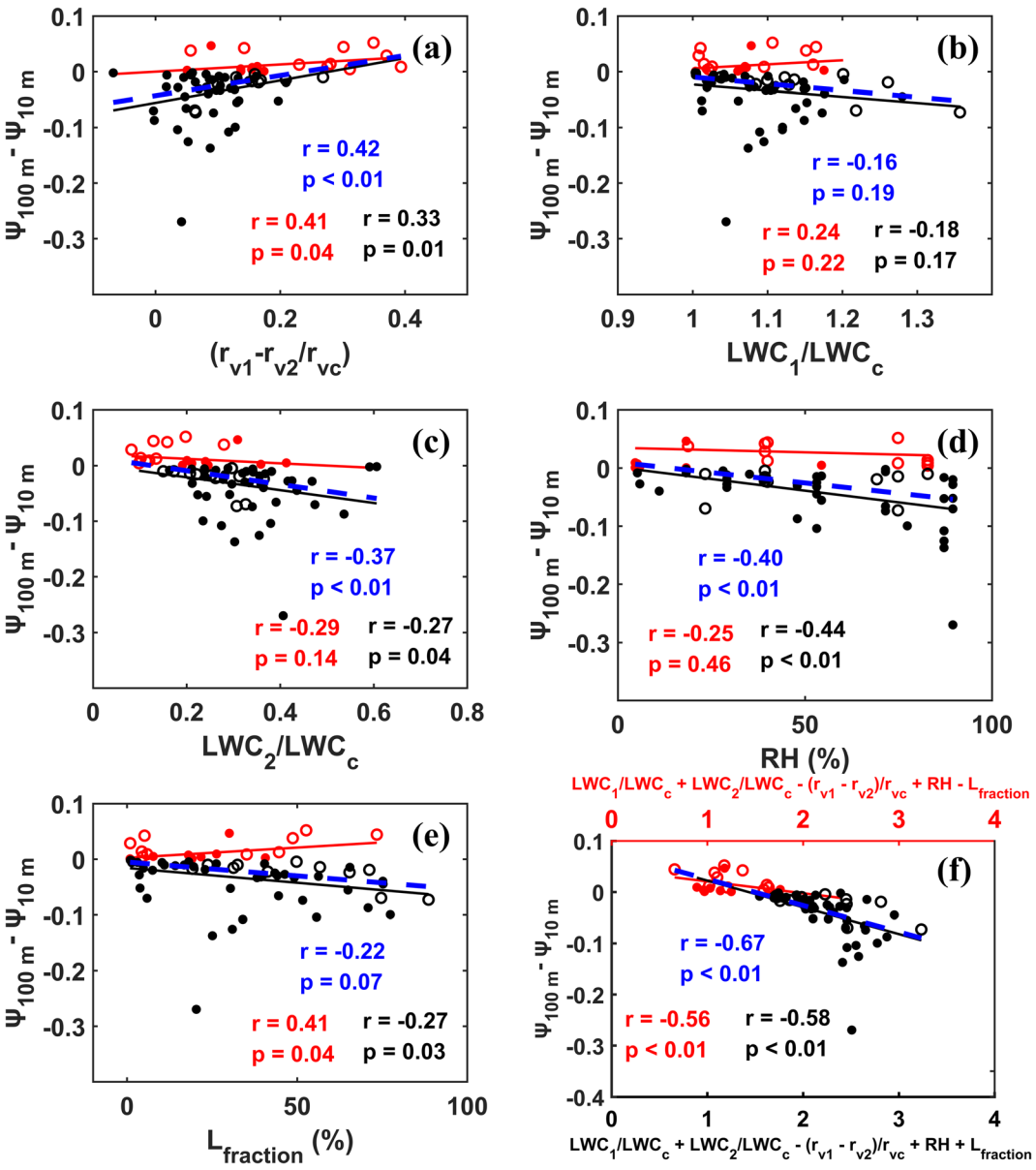

Figure 3. Scale dependence strength ($\psi_{100m} - \psi_{10m}$) as a function of (a) $(r_{v1} - r_{v1})/r_{vc}$, (b) LWC_1/LWC_c, (c) LWC_2/LWC_c, (d) RH, (e) $L_{fraction}$, and (f) $LWC_1/LWC_c + LWC_2/LWC_c + RH - (r_{v1} - r_{v2})/r_{vc} - L_{fraction}$ for the 18 INCREASE legs (red) and $LWC_1/LWC_c + LWC_2/LWC_c + RH - (r_{v1} - r_{v2})/r_{vc} + L_{fraction}$ for the 51 DECREASE legs (black) during ACE-ENA (solid points) and RACORO (open points). The blue lines represent the fitting with both the INCREASE and DECREASE legs. Each legend provides the correlation coefficients (r) and the p values of the correlations. See text for the meanings of the symbols.

Figure 3 are still the same as those in Figure S3 except for $\psi_{100m} - \psi_{10m}$ versus LWC_1/LWC_c. Some correlation coefficients are small, and/or some p values are larger than 0.05, especially for the INCREASE legs. One reason is that when the relationship between $\psi_{100m} - \psi_{10m}$ and each factor is considered separately, the points are scattered because of the influences of other factors, which is explained in Text S2 of the supporting information by taking $\psi_{100m} - \psi_{10m}$ versus LWC_1/LWC_c as an example. The other reason could be the limited number of data points, especially for the INCREASE legs.

In order to consider all the factors, two new dimensionless parameters combining all the factors are introduced to quantify the scale dependence further: $LWC_1/LWC_c + LWC_2/LWC_c - (r_{v1} - r_{v2})/r_{vc} + RH - L_{fraction}$ for the INCREASE legs and $LWC_1/LWC_c + LWC_2/LWC_c - (r_{v1} - r_{v2})/$

r_{vc} + RH + $L_{fraction}$ for the DECREASE legs. The correlation coefficients in Figure 3f are, respectively, larger than those in Figures 3a–3e for the INCREASE, DECREASE, and INCREASE + DECREASE legs, providing observational evidence supporting the utilities of the new dimensionless parameters. More studies with additional observations are needed to substantiate the results.

The above results suggest that smaller $(r_{v1} - r_{v2})/r_{vc}$ and larger LWC_1/LWC_c, LWC_2/LWC_c, and RH tend to cause $k_{24} < k_{23}$ and the entrainment-mixing mechanisms closer to extreme inhomogeneous mixing for a larger averaging scale. Such a variation of entrainment-mixing mechanism becomes weaker or even the mechanism becomes more homogeneous, for larger $(r_{v1} - r_{v2})/r_{vc}$ and smaller LWC_1/LWC_c, LWC_2/LWC_c, and RH, with less negative $k_{24} - k_{23}$ or even $k_{24} > k_{23}$. Meanwhile, $L_{fraction}$ can only affect the strength of scale dependence but not its sign.

The mechanisms responsible for the effects of $(r_{v1} - r_{v2})/r_{vc}$, LWC_1/LWC_c, LWC_2/LWC_c, RH, and $L_{fraction}$ are further examined in two different ways using the heuristic model. First, the sign and strength of scale dependence are determined by the variation of line slopes $(k_{24} - k_{23})$ in Figure 1. Text S3 and Figure S6 show how these factors affect scale dependence in detail. Take the effect of $(r_{v1} - r_{v2})/r_{vc}$ as an example (Figures S6a and S6b). When $(r_{v1} - r_{v2})/r_{vc} < 0$, $\psi_{100m} - \psi_{10m}$ and $k_{24} - k_{23}$ must be negative. When $(r_{v1} - r_{v2})/r_{vc} > 0$, $\psi_{100m} - \psi_{10m}$ and $k_{24} - k_{23}$ can be positive or negative, which depends on "competitive" opposite effects of $(r_{v1} - r_{v2})/r_{vc}$, LWC_1/LWC_c, and LWC_2/LWC_c. No matter in which scenario, $\psi_{100m} - \psi_{10m}$ is always positively correlated with $(r_{v1} - r_{v2})/r_{vc}$. The effects of LWC_1/LWC_c, LWC_2/LWC_c, RH, and $L_{fraction}$ are also explained with k_{24} and k_{23} in a similar way.

Second, whether scale dependence is positive or negative is determined by whether ψ of CDSDs near droplet-free air is larger or smaller than that far away. For the INCREASE legs, the mean ψ_2 (0.69) of CDSDs near dry air is larger than the mean ψ_1 (0.63) far away at the resolution of 10 m. Another crucial factor is that the CDSDs near dry air play a more important role than those far away. The ratio of the weights of r_{v2} and r_{v1} for r_{vc100m} is $\frac{100}{100 - S}$ times that for r_{vc10m} (equations (S1), (S3), and (S5)). Since the ratio of the weights of LWC_2 and LWC_1 is the same for the 10 and 100 m resolutions (equations (S2) and (S4)), only the ratio for r_{vc100m} needs to be considered. Because $\psi_2 > \psi_1$ and the role of ψ_2 is amplified for the 100 m resolution, ψ is larger at the 100 m resolution than that at the 10 m resolution. For similar reasons, ψ is smaller at the 100 m resolution than at the 10 m resolution for the DECREASE legs, because ψ_2 (0.69) < ψ_1 (0.78). The mean $\psi_2 - \psi_1$ along the INCREASE legs (0.06) is two thirds of the absolute value of mean $\psi_2 - \psi_1$ along the DECREASE legs (−0.09). In addition, the weight $\frac{100}{100 - \frac{S}{10}}$ is related to $L_{fraction}$ (equation (S8)); the larger the S and $L_{fraction}$, the larger the amplification. The mean $L_{fraction}$ along the INCREASE legs (0.24) is two thirds of that along the DECREASE legs (0.36). Therefore, the mean $\psi_{100m} - \psi_{10m}$ along the INCREASE legs (0.02) is smaller than the absolute value of mean $\psi_{100m} - \psi_{10m}$ along the DECREASE legs (−0.04). The analysis also supports that microphysics and RH affect both sign and strength of scale dependence, but $L_{fraction}$ only affects the strength.

Also, the absolute mean $\psi_{100m} - \psi_{10m}$ (−0.04) for the DECREASE legs is much smaller than that in the cumulus clouds (−0.15) in Lu et al. (2014). The reason is that the mean ψ_1 and ψ_2 are 0.93 and 0.51, respectively, in Lu et al. (2014); therefore, the absolute value of negative $\psi_2 - \psi_1$ (−0.42) is much larger than that in this study (−0.09). The stratocumulus clouds in this study have both weak negative and positive scale dependence behaviors. In future studies, more data need to be examined strong negative and positive scale dependence.

4. Concluding Remarks

This study addresses the understudied topic, scale dependence of entrainment-mixing processes, which is critical to developing scale-aware parameterizations of entrainment mixing. Measurements of the stratocumulus clouds during the ACE-ENA and RACORO campaigns are analyzed to study the scale dependence of entrainment-mixing mechanisms. Two opposite scale dependence behaviors are found in both campaigns, different from previous studies (Burnet & Brenguier, 2007; Lu et al., 2014). Homogeneous mixing degree decreases along 51 legs and increases along the other 18 legs, when the averaging distance/time increases. The two opposite scale dependence behaviors can be well fitted by power law functions.

It is found that the scale dependence of ψ is closely related to microphysics, relative humidity of entrained dry air, and droplet-free air blob sizes. It is interesting to note that not only the microphysics near droplet-free air but also the microphysics far away from droplet-free air are important to the scale dependence, while Lu et al. (2014) only emphasized the importance of microphysics near droplet-free air.

A new heuristic model is presented to illustrate the observational results. Based on the heuristic model, the physical mechanisms responsible for the different scale dependence behaviors are further examined in two different ways. First, the sign and strength of scale dependence are determined by the variation of line slopes in the mixing diagram. The significant difference between mean volume radius far away from droplet-free air and that nearby can enhance the positive scale dependence and weaken the negative one. The large liquid water content near and/or far away from dry air and large relative humidity of the entrained air enhance the negative scale dependence and weaken the positive one. Differently, the large droplet-free air fraction can enhance both positive and negative scale dependence. All the factors can affect scale dependence at the same time; therefore, two new dimensionless parameters combining all the factors are defined to better quantify their combined effects on scale dependence.

Second, the sign and strength of scale dependence are determined by local homogeneous mixing degree and weights of CDSDs near and far away from dry air. For the positive scale dependence, homogeneous mixing degree near dry air is larger than that far away. The scenario is opposite for the negative scale dependence. The positive or negative scale dependence strength can be amplified by increasing droplet-free air fraction, because the CDSDs near dry air have a larger weight than those far away and the weight increases with the increasing droplet-free air fraction.

Therefore, the microphysics near and far away from droplet-free air and relative humidity of the entrained air determine both the sign and strength of scale dependence, while droplet-free air fraction only determines the strength. This conclusion is more general than what has been reported in the literature (Burnet & Brenguier, 2007; Lu et al., 2011). More studies with additional observations need to be substantiated the results.

Acknowledgments
This research is supported by the National Key Research and Development Program of China (2017YFA0604001), the Natural Science Foundation of Jiangsu Province (BK20160041), the National Natural Science Foundation of China (41822504, 91537108 and 41975181), the Qinglan Project (R2018Q05), and the Six Talent Peak Project in Jiangsu (2015-JY-011). Y. Liu is supported by the U.S. Department of Energy Atmospheric System Research (ASR) program (DE-SC00112704) and Solar Energy Technologies Office (SETO) under Award 33504. The ACE-ENA data are available from https://www.arm.gov/research/campaigns/aaf2017ace-ena, and the RACORO data are available from https://www.arm.gov/research/campaigns/aaf2009racoro website.

References

Ackerman, A. S., Kirkpatrick, M. P., Stevens, D. E., & Toon, O. B. (2004). The impact of humidity above stratiform clouds on indirect aerosol climate forcing. *Nature*, *432*(7020), 1014–1017. https://doi.org/10.1038/nature03174

Bony, S., & Dufresne, J. L. (2005). Marine boundary layer clouds at the heart of tropical cloud feedback uncertainties in climate models. *Geophysical Research Letters*, *32*, L20806. https://doi.org/10.1029/2005GL023851

Burnet, F., & Brenguier, J.-L. (2007). Observational study of the entrainment-mixing process in warm convective clouds. *Journal of the Atmospheric Sciences*, *64*(6), 1995–2011. https://doi.org/10.1175/JAS3928.1

Cess, R. D., Potter, G., Blanchet, J., Boer, G., Ghan, S., Kiehl, J., et al. (1989). Interpretation of cloud-climate feedback as produced by 14 atmospheric general circulation models. *Science*, *245*(4917), 513–516. https://doi.org/10.1126/science.245.4917.513

Chosson, F., Brenguier, J.-L., & Schüller, L. (2007). Entrainment-mixing and radiative transfer simulation in boundary layer clouds. *Journal of the Atmospheric Sciences*, *64*(7), 2670–2682. https://doi.org/10.1175/JAS3975.1

Del Genio, A. D., & Wu, J. (2010). The role of entrainment in the diurnal cycle of continental convection. *Journal of Climate*, *23*(10), 2722–2738. https://doi.org/10.1175/2009JCLI3340.1

Diskin, G. S., Podolske, J. R., Sachse, G. W., & Slate, T. A. (2002). *Open-path airborne tunable diode laser hygrometer, paper presented at proceedings of SPIE*. Wash: Seattle.

Freud, E., Rosenfeld, D., Andreae, M., Costa, A., & Artaxo, P. (2008). Robust relations between CCN and the vertical evolution of cloud drop size distribution in deep convective clouds. *Atmospheric Chemistry and Physics*, *8*(6), 1661–1675.

Freud, E., Rosenfeld, D., & Kulkarni, J. R. (2011). Resolving both entrainment-mixing and number of activated CCN in deep convective clouds. *Atmospheric Chemistry and Physics*, *11*(24), 12,887–12,900. https://doi.org/10.5194/acp-11-12887-2011

Gerber, H. E., Frick, G. M., Jensen, J. B., & Hudson, J. G. (2008). Entrainment, mixing, and microphysics in trade-wind cumulus. *Journal of the Meteorological Society of Japan*, *86A*, 87–106. https://doi.org/10.2151/jmsj.86A.87

Grabowski, W. W. (2006). Indirect impact of atmospheric aerosols in idealized simulations of convective–radiative quasi equilibrium. *Journal of Climate*, *19*(18), 4664–4682. https://doi.org/10.1175/JCLI3857.1

Haman, K. E., Malinowski, S. P., Kurowski, M. J., Gerber, H., & Brenguier, J.-L. (2007). Small scale mixing processes at the top of a marine stratocumulus—A case study. *Quarterly Journal of the Royal Meteorological Society*, *133*(622), 213–226. https://doi.org/10.1002/qj.5

Hill, A. A., Feingold, G., & Jiang, H. (2009). The influence of entrainment and mixing assumption on aerosol–cloud interactions in marine stratocumulus. *Journal of the Atmospheric Sciences*, *66*(5), 1450–1464. https://doi.org/10.1175/2008jas2909.1

Hoffmann, F., & Feingold, G. (2019). Entrainment and mixing in stratocumulus: Effects of a new explicit subgrid-scale scheme for large-eddy simulations with particle-based microphysics. *Journal of the Atmospheric Sciences*, *76*(7), 1955–1973. https://doi.org/10.1175/jas-d-18-0318.1

Jensen, J., Austin, P., Baker, M., & Blyth, A. (1985). Turbulent mixing, spectral evolution and dynamics in a warm cumulus cloud. *Journal of the Atmospheric Sciences*, *42*(2), 173–192. https://doi.org/10.1175/1520-0469(1985)042<0173:TMSEAD>2.0.CO;2

Jeworrek, J., West, G., & Stull, R. (2019). Evaluation of cumulus and microphysics parameterizations in WRF across the convective gray zone. *Weather and Forecasting*, *34*(4), 1097–1115.

Kim, B. G., Miller, M. A., Schwartz, S. E., Liu, Y., & Min, Q. (2008). The role of adiabaticity in the aerosol first indirect effect. *Journal of Geophysical Research*, *113*, D05210. https://doi.org/10.1029/2007JD008961

Kumar, B., Götzfried, P., Suresh, N., Schumacher, J., & Shaw, R. A. (2018). Scale dependence of cloud microphysical response to turbulent entrainment and mixing. *Journal of Advances in Modeling Earth Systems*, *10*(11), 2777–2785. https://doi.org/10.1029/2018ms001487

Kumar, B., Schumacher, J., & Shaw, R. A. (2013). Cloud microphysical effects of turbulent mixing and entrainment. *Theoretical and Computational Fluid Dynamics*, *27*(3–4), 361–376. https://doi.org/10.1007/s00162-012-0272-z

Lasher-trapp, S. G., Cooper, W. A., & Blyth, A. M. (2005). Broadening of droplet size distributions from entrainment and mixing in a cumulus cloud. *Quarterly Journal of the Royal Meteorological Society*, *131*(605), 195–220. https://doi.org/10.1256/qj.03.199

Lehmann, K., Siebert, H., & Shaw, R. A. (2009). Homogeneous and inhomogeneous mixing in cumulus clouds: Dependence on local turbulence structure. *Journal of the Atmospheric Sciences*, *66*(12), 3641–3659. https://doi.org/10.1175/2009jas3012.1

Liu, Y., Daum, P. H., Chai, S. K., & Liu, F. (2002). Cloud parameterizations, cloud physics, and their connections: An overview. *Recent Res. Geoscientific Model Development*, *4*, 119–142.

Lu, C., Liu, Y., & Niu, S. (2011). Examination of turbulent entrainment-mixing mechanisms using a combined approach. *Journal of Geophysical Research*, *116*, D20207. https://doi.org/10.1029/2011JD015944

Lu, C., Liu, Y., Niu, S., & Endo, S. (2014). Scale dependence of entrainment-mixing mechanisms in cumulus clouds. *Journal of Geophysical Research: Atmospheres*, *119*, 13,877–813,890. https://doi.org/10.1002/2014JD022265

Lu, C., Liu, Y., Yum, S. S., Niu, S., & Endo, S. (2012). A new approach for estimating entrainment rate in cumulus clouds. *Geophysical Research Letters*, *39*, L04802. https://doi.org/10.1029/2011gl050546

Lu, C., Niu, S., Liu, Y., & Vogelmann, A. M. (2013). Empirical relationship between entrainment rate and microphysics in cumulus clouds. *Geophysical Research Letters*, *40*, 2333–2338. https://doi.org/10.1002/grl.50445

Morrison, H., & Grabowski, W. W. (2008). Modeling supersaturation and subgrid-scale mixing with two-moment bulk warm microphysics. *Journal of the Atmospheric Sciences*, *65*(3), 792–812. https://doi.org/10.1175/2007jas2374.1

Pawlowska, H., Brenguier, J., & Burnet, F. (2000). Microphysical properties of stratocumulus clouds. *Atmospheric Research*, *55*(1), 15–33. https://doi.org/10.1016/S0169-8095(00)00054-5

Slawinska, J., Grabowski, W. W., Pawlowska, H., & Morrison, H. (2012). Droplet activation and mixing in large-eddy simulation of a shallow cumulus field. *Journal of the Atmospheric Sciences*, *69*(2), 444–462. https://doi.org/10.1175/jas-d-11-054.1

Stanfield, R. E., Su, H., Jiang, J. H., Freitas, S. R., Molod, A. M., Luo, Z. J., et al. (2019). Convective entrainment rates estimated from Aura CO and CloudSat/CALIPSO observations and comparison with GEOS-5. *Journal of Geophysical Research: Atmospheres*, *124*, 9796–9807. https://doi.org/10.1029/2019JD030846

Stephens, G. L. (2005). Cloud feedbacks in the climate system: A critical review. *Journal of Climate*, *18*(2), 237–273. https://doi.org/10.1175/JCLI-3243.1

Su, C.-W., Krueger, S. K., McMurtry, P. A., & Austin, P. H. (1998). Linear eddy modeling of droplet spectral evolution during entrainment and mixing in cumulus clouds. *Atmospheric Research*, *47*, 41–58. https://doi.org/10.1016/S0169-8095(98)00039-8

Vogelmann, A., McFarquhar, G., Ogren, J., Turner, D., Comstock, J., Feingold, G., et al. (2012). RACORO extended-term aircraft observations of boundary layer clouds. *Bulletin of the American Meteorological Society*, *93*(6), 861–878. https://doi.org/10.1175/BAMS-D-11-00189.1

Wang, Y. (2015). *Aerosol-cloud interactions from urban, regional, to global scales*. Berlin: Springer.

Xie, X., & Zhang, M. (2015). Scale-aware parameterization of liquid cloud inhomogeneity and its impact on simulated climate in CESM. *Journal of Geophysical Research: Atmospheres*, *120*, 8359–8371. https://doi.org/10.1002/2015JD023565

Xue, H., & Feingold, G. (2006). Large-eddy simulations of trade wind cumuli: Investigation of aerosol indirect effects. *Journal of the Atmospheric Sciences*, *63*(6), 1605–1622. https://doi.org/10.1175/JAS3706.1

Yang, F., Shaw, R., & Xue, H. (2016). Conditions for super-adiabatic droplet growth after entrainment mixing. *Atmospheric Chemistry and Physics*, *16*(14), 9421–9433. https://doi.org/10.5194/acp-2016-94

Yang, Y., Zhao, C., Dong, X., Fan, G., Zhou, Y., Wang, Y., et al. (2019). Toward understanding the process-level impacts of aerosols on microphysical properties of shallow cumulus cloud using aircraft observations. *Atmospheric Research*, *221*, 27–33. https://doi.org/10.1016/j.atmosres.2019.01.027

Yeom, J. M., Yum, S. S., Liu, Y., & Lu, C. (2017). A study on the entrainment and mixing process in the continental stratocumulus clouds measured during the RACORO campaign. *Atmospheric Research*, *194*, 89–99. https://doi.org/10.1016/j.atmosres.2017.04.028

Yum, S. S. (1998). *Cloud droplet spectral broadening in warm clouds: An observational and model study, dissertation for the doctoral degree thesis*. Reno: Univ. of Nev.

Yun, Y., Fan, J., Xiao, H., Zhang, G. J., Ghan, S. J., Xu, K.-M., et al. (2017). Assessing the resolution adaptability of the Zhang-McFarlane cumulus parameterization with spatial and temporal averaging. *Journal of Advances in Modeling Earth Systems*, *9*(7), 2753–2770.

Zheng, Y., Rosenfeld, D., & Li, Z. (2015). Sate llite inference of thermals and cloud-base updraft speeds based on retrieved surface and cloud-base temperatures. *Journal of the Atmospheric Sciences*, *72*(6), 2411–2428. https://doi.org/10.1175/JAS-D-14-0283.1